

# Super LiDAR Reflectance for Robotic Perception

Wei Gao<sup>1</sup>, Jie Zhang<sup>1</sup>, Mingle Zhao<sup>1</sup>, Zhiyuan Zhang<sup>2</sup>, Shu Kong<sup>1</sup>, Maani Ghaffari<sup>3</sup>,  
Dezhen Song<sup>4</sup>, Cheng-Zhong Xu<sup>1</sup>, and Hui Kong<sup>1</sup>

**Abstract**—Conventionally, human intuition often defines *vision* as a modality of passive optical sensing, while active optical sensing is typically regarded as measuring rather than the default modality of vision. However, the situation now changes: sensor technologies and data-driven paradigms empower active optical sensing to redefine the boundaries of vision, ushering in a new era of *active vision*. Light Detection and Ranging (LiDAR) sensors capture reflectance from object surfaces, which remains invariant under varying illumination conditions, showcasing significant potential in robotic perception tasks such as detection, recognition, segmentation, and Simultaneous Localization and Mapping (SLAM). These applications often rely on dense sensing capabilities, typically achieved by high-resolution, expensive LiDAR sensors. A key challenge with low-cost LiDARs lies in the sparsity of scan data, which limits their broader application. To address this limitation, this work introduces an innovative framework for generating dense LiDAR reflectance images from sparse data, leveraging the unique attributes of non-repeating scanning LiDAR (NRS-LiDAR). We tackle critical challenges, including reflectance calibration and the transition from static to dynamic scene domains, facilitating the reconstruction of dense reflectance images in real-world settings. The key contributions of this work include a comprehensive dataset for LiDAR reflectance image densification, a densification network tailored for NRS-LiDAR, and diverse applications such as loop closure and traffic lane detection using the generated dense reflectance images. Experimental results validate the efficacy of the proposed approach, which successfully integrates computer vision techniques with LiDAR data processing, enhancing the applicability of low-cost LiDAR systems and establishing a novel paradigm for robotic active vision—*LiDAR as a Camera*. The dataset and code are available at: To Be Updated.

## I. INTRODUCTION

Recent advancements in LiDAR technology have greatly enhanced its accessibility, driven by reductions in sensor size and cost, thereby expanding its applicability across a wide range of robotic applications. In addition to delivering precise 3D spatial data, LiDAR systems are capable of capturing reflectance intensity from objects' surfaces, acquiring

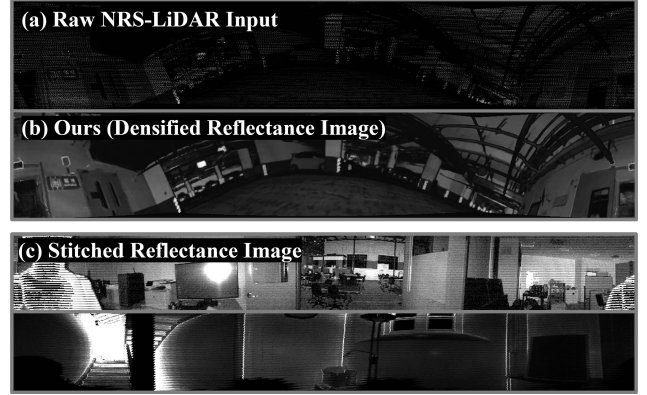


Fig. 1. Comparison between the reflectance image densified by the proposed method and the true reflectance images stitched from high-line LiDAR data. (a) Raw NRS-LiDAR input. (b) Densified  $1380 \times 240$  reflectance image using the proposed method. (c) Stitched  $1024 \times 128$  reflectance images using the high-cost Ouster 128-line LiDAR data from [1], [2]. Thanks to the proposed network and NRS-LiDARs, the method effectively eliminates line artifacts and mitigates overexposure in challenging scenarios, generating high-definition, camera-grade reflectance images.

illumination-invariant environmental information, and rich texture to complement the limitations of pure geometric-based LiDAR sensing.

To date, numerous studies have used LiDAR reflectance intensity for a variety of applications, including loop closure detection [2]–[4], intensity-enhanced LiDAR odometry [1], [5]–[7], segmentation [8], [9], and object detection [10], [11]. These applications typically depend on dense reflectance images, which are often generated by high-resolution, costly LiDAR sensors such as the Ouster OS1-128 and Velodyne VLS-128. In contrast, low-cost LiDAR sensors, such as the Velodyne-16, Velodyne-32, or Livox MID-360, generally produce sparse data, posing significant challenges for directly applying methods designed for dense reflectance images.

Intuitively, generating dense and accurate reflectance images from sparse LiDAR data holds significant potential to advance robotic perception tasks, yet this area remains under-explored in existing research [12]. Successfully tackling this challenge would effectively bridge the gap between computer vision techniques and LiDAR data, facilitating the adaptation of camera-based methodologies to LiDAR systems. Moreover, it would address the inherent limitations of traditional cameras, such as their sensitivity to lighting conditions, while simultaneously enhancing the texture representation capabilities of LiDAR technology.

Creating dense LiDAR reflectance images typically depends on high-quality, high-resolution ground-truth data, particularly when using deep neural networks. However,

<sup>1</sup>Wei Gao, Jie Zhang, Mingle Zhao, Shu Kong, Chengzhong Xu, and Hui Kong are with the State Key Laboratory of Internet of Things for Smart City (SKL-IOTSC), Faculty of Science and Technology, University of Macau, Macau. ({gw.ga0.wei, mc25934, zhao.mingle}@connect.um.edu.mo, {skong, czxu, huikong}@um.edu.mo)

<sup>2</sup>Zhiyuan Zhang is with the School of Computing and Information Systems, Singapore Management University, Singapore. (zhiyuanzhang@smu.edu.sg)

<sup>3</sup>Maani Ghaffari is with the Department of Naval Architecture and Marine Engineering and Department of Robotics, University of Michigan, Ann Arbor, MI, USA. (maanigj@umich.edu)

<sup>4</sup>Dezhen Song is with the Department of Robotics, Mohamed bin Zayed University of Artificial Intelligence (MBZUAI), UAE. (dezhen.song@mbzuai.ac.ae)

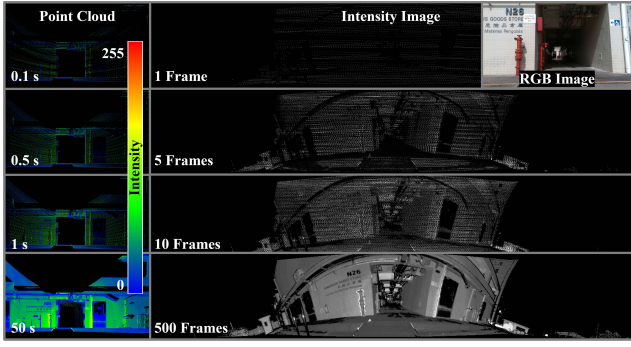


Fig. 2. Illustration of the non-repeating scanning mechanism. When stationary, the LiDAR gradually produces denser point clouds over time within the same FoV, allowing the reflectance intensity image derived from the point cloud projection to achieve higher density as well. The color of point clouds or gray-scale images represents the intensity value.

acquiring such data often requires specialized sensors or configurations, posing significant challenges. In this study, we capitalize on the distinctive imaging properties of NRS-LiDAR to produce high-quality ground-truth reflectance images (Fig. 1). As shown in Fig. 2, dense ground-truth data can be acquired in static environments through scan accumulation. Nevertheless, acquiring dense ground-truth data is not feasible when the robot is in motion. In dynamic scenarios, sparse and rapidly changing inputs must be processed in real time, significantly increasing the complexity of dense reconstruction. The disparity between static ground-truth generation and dynamic scene processing underscores the challenges of achieving dense reflectance images with low-cost LiDARs. In summary, we face two challenging issues. The first is to acquire dense ground-truth for reflectance image densification in motion conditions. The second issue is how to densify the sparse reflectance given ground-truth data. To address these issues, we propose a novel method that includes the following contributions:

- 1) We propose the first benchmark dataset tailored for LiDAR reflectance image densification. Compare to existing LiDAR datasets [1], [13], our dataset providing paired sparse-to-dense ground truth data, enabling both end-to-end deep learning based densification benchmarking and image-level perception tasks.
- 2) We introduce a novel convolutional network specifically designed for real-time densification of the reflectance image of NRS-LiDAR (e.g., Livox MID-360). Our approach effectively addresses two critical challenges: the static-to-motion domain gap and adaptive intensity calibration in LiDAR reflectance image densification. Compared to existing methods, our method achieves significant improvements in quality and accuracy.
- 3) We validate the effectiveness of the densified reflectance image in loop closure and traffic lane detection, achieving significant improvement under challenging conditions and demonstrating its potential to enhance practical applications of low-cost LiDAR systems.

## II. RELATED WORKS

### A. LiDAR Reflectance in Robotics

In single LiDAR-based applications, numerous studies have primarily focused on exploiting geometric information for robotic perception [14] and localization [15] tasks. Nevertheless, these approaches exhibit limitations in geometrically degenerated environments due to their inability to capture texture information. To address this, researchers have explored fusing camera and LiDAR data to exploit their complementary strengths [16], [17]. However, this integration presents challenges, including additional hardware requirements, precise calibration, and temporal synchronization. Moreover, visual sensors are inherently limited by illumination conditions.

A promising alternative focuses on leveraging LiDAR's intrinsic reflectance properties. Significant progress has been demonstrated in this domain. A loop closure detection method that synergistically combines geometric and intensity data is proposed [18]. Furthermore, the application of reflectance information has proven particularly effective in robotic terrain analysis, enabling semantic segmentation to distinguish between road surfaces and grasslands [19].

Recently, dense reflectance images, which are generated by high-resolution LiDAR sensors, have been utilized to enhance robotic perception capabilities [5], [6]. A notable work is COIN-LIO [1], which is a LiDAR-inertial odometry framework integrating photometric error minimization on LiDAR intensity images with geometric registration to address challenges in geometrically degenerated environments. A hybrid loop closure detection method is introduced in [2] by combining LiDAR point cloud and LiDAR intensity image, achieving superior robustness. However, these advanced methods rely on high-resolution, high-cost LiDAR sensors, making them impractical for low-cost applications and emphasizing the need for alternative strategies in resource-constrained scenarios.

This study presents a novel approach of reconstructing high-fidelity dense reflectance images from sparse ones with low-cost LiDAR sensors, and demonstrates significant potential in real-world real-time robot applications.

### B. Depth Completion

Dense environmental sensing is critical for robotic tasks. However, physical sensors typically provide only sparse measurements. Completing sparse sensory data into dense perceptual representations is thus a crucial research direction. Depth completion [20], [21] is one of the most extensively studied domains, inspiring us to review dense completion methods. Depth completion utilizes sparse depth data from sensor measurements [22]–[25], multi-view geometry [26], [27], or data-driven priors [28], [29], to generate dense depth images, enabling continuous and dense perception for navigation and manipulation.

However, directly applying existing depth completion approaches to LiDAR reflectance images densification is challenging due to the complexities of intensity measure-

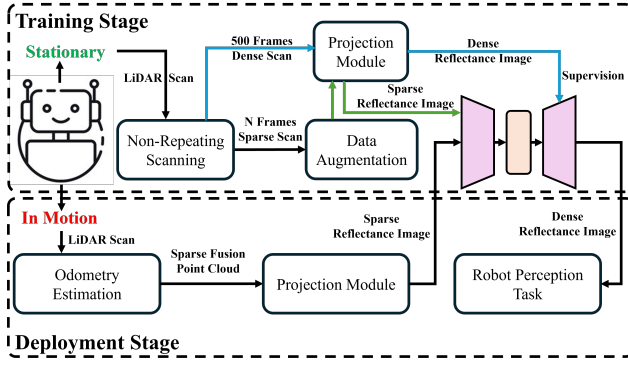


Fig. 3. System diagram: During stationary, the robot utilizes NRS-LiDAR to obtain sparse and dense LiDAR data. Sparse data is augmented to simulate motion characteristics, while dense data serves as supervision to train a reflectance image densification network for motion perception tasks.

ments. Factors such as incidence angle, surface reflectance properties, and sensor-to-target distance [30] complicate the learning of latent intensity patterns, especially with limited public training data available. Therefore, developing novel networks specifically for LiDAR reflectance images densification is essential. Unlike depth completion, which focuses solely on geometry, LiDAR reflectance images densification equips robots with a new, high-resolution eye, thus allowing high-level visual perception to be achieved through LiDAR, opening the door to reimagining various vision problems.

### III. METHODOLOGY

Robots in motion often require sufficient time to accumulate data for a comprehensive understanding of their environment. In this section, we detail our proposed method to address this challenge. As shown in Fig. 3, the purpose of this work is to rely solely on sparse LiDAR data collected by the robot over a short period during motion as input to generate dense and accurate reflectance images as output, providing comprehensive environmental information for robotic perception tasks.

#### A. Dataset Construction

1) *Data Acquisition:* The Super LiDAR Reflectance dataset was acquired using a Giraffe ground robot platform equipped with a multi-sensor suite: an Intel RealSense D435i camera capturing RGB images at  $1280 \times 720$  resolution, a Livox MID-360 LiDAR sensor with a  $360^\circ$  horizontal and  $59^\circ$  vertical field of view (FoV) operating at 10 Hz point cloud generation rate, and a high-frequency IMU sampling at 200 Hz. Initially, the robot autonomously navigated through selected representative environments. Upon reaching predetermined locations, it maintained a stationary pose for 60 seconds to facilitate the accumulation of multiple LiDAR scans. The synchronized sensor data, including LiDAR point clouds, camera images, and IMU measurements, were recorded as raw ROS (Robot Operating System) packets and systematically organized into dataset collections. To ensure data diversity and minimize inter-dataset correlation, the robot's orientation and position were deliberately adjusted between recording sessions, thereby maintaining the independence and representativeness of each dataset instance.

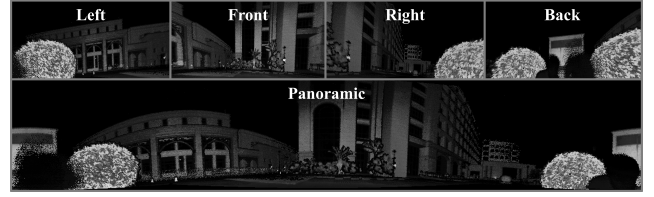


Fig. 4. Reflectance images obtained by virtual-camera projection mode (top) and panoramic mode (bottom), respectively, when the NRS-LiDAR is placed at a preset location for 60 seconds.

2) *Ground Truth Generation:* This section exploits two projection methods to generate ground-true LiDAR reflectance image: panoramic spherical projection and virtual-camera perspective projection. In the former one, LiDAR points are directly mapped onto a spherical surface. The azimuth  $\theta = \arctan 2(y, x)$  and elevation  $\phi = \arctan 2\left(z, \sqrt{x^2 + y^2}\right)$  of a specific 3D point are converted into 2D coordinates:  $\text{col} = \left\lfloor \frac{-\theta + 180^\circ}{360^\circ} \cdot W \right\rfloor$  and  $\text{row} = \left\lfloor \frac{\phi_{\max} - \phi}{\phi_{\max} - \phi_{\min}} \cdot H \right\rfloor$  where  $W$  and  $H$  are the width and height of the generated image.  $[\phi_{\min}, \phi_{\max}]$  defines the vertical FoV. The intensity  $I$  is assigned to the corresponding pixel (row, col). This method aligns with the LiDAR sensor's FoV, producing images with a resolution of  $1380 \times 240$  pixels.

In the virtual-camera perspective projection, four virtual cameras are placed around the LiDAR sensor to project the point cloud into four views. Using a pinhole camera model, 3D points  $(x, y, z)$  are mapped onto a 2D image plane,

$$\text{col} = \left\lfloor -f_x \frac{y}{x} + c_x \right\rfloor, \quad (1)$$

$$\text{row} = \left\lfloor H - 1 - \frac{\arctan 2(z, x) - \phi_{\min}}{\phi_{\max} - \phi_{\min}} \cdot H \right\rfloor, \quad (2)$$

where  $f_x = \frac{W}{2 \cdot \tan(\frac{\text{horizontal FoV}}{2})}$ ,  $f_y = \frac{H}{\phi_{\max} - \phi_{\min}}$ , and  $c_x = \frac{W}{2}$ . Each view generates reflectance images with a resolution of  $240 \times 480$  pixels.

The exemplar reflectance images generated by these two projection modes are shown in Fig. 4. Since the density of LiDAR reflectance image varies with the number of accumulated scans, we use reflectance images accumulated over 500 scans as ground-truth to provide supervision during the training process. Through the aforementioned data acquisition, we constructed the Super LiDAR Reflectance dataset, which includes 1,000 raw ROS packets (600K frames) and an additional 5,000 sets of reflectance images ranging from sparse (1 scan) to dense (500 scans) configuration, covering diverse urban environments such as residential areas, streets, parking lot and intersections. The dataset also includes two test subsets targeting specific applications of dense reflectance images: one is for loop closure detection, with data from three scenarios at two time intervals of day (morning, evening), using panoramic spherical projection for robust matching across different viewpoints. The other subset is designed for lane detection under varying traffic scenarios during the day and night, where the virtual-camera perspective projection is used (more suitable for this task).

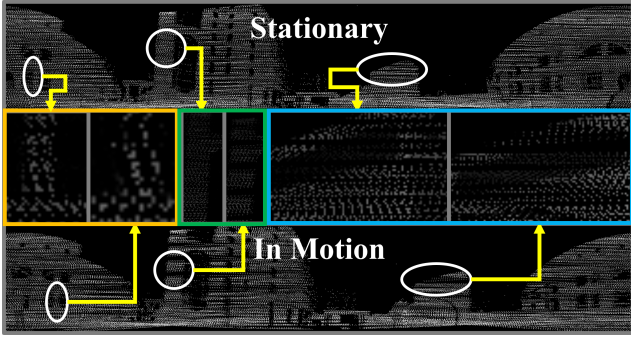


Fig. 5. Comparison of reflectance images fused from 5 scans in stationary and in-motion cases. The image shows the corresponding reflectance images. In the stationary case, the 5-scan inputs are aligned, whereas the in-motion case reveals irregularities and misalignment due to motions.

### B. Static-to-Dynamic Domain Gap

The above ground-truth supervision data collection is collected when the LiDAR is stationary. However, the proposed reflectance densification method is generally intended for robot perception tasks when the LiDAR is in-motion. In practical motion mode, it is necessary to fuse via odometry estimation a certain number of consecutive scans to construct a relatively dense reflectance image as network input. When fusing, using too few scans (e.g., only one or two scans) often results in excessively sparse data, leading to lacking sufficient information. On the other hand, fusing too many scans can introduce errors caused by odometry estimation inaccuracies or noise points generated by dynamic objects in the scene. To address the influence of dynamic objects in such scenarios, we adopt the preprocessing method proposed in [31] to filter the raw point cloud data, effectively removes motion artifacts caused by dynamic objects and mitigating their adverse effects on the fusion process. In our case, the network input is generated by fusing  $N$  (a small number) consecutive scans using odometry estimates obtained by [15]. By comparing with the static ground-truth training data generation, there obviously exists a gap between the static training data and dynamic inference ones, which can degrade performance during motion scenario.

As shown in Fig. 5, the key differences can be described in two aspects. *geometric misalignment*: Odometry-based scan fusion during motion introduces alignment errors due to cumulative motion estimation inaccuracies, leading to inconsistencies in the input. *Motion-induced distribution shift*: Robot motion alters the data distribution, leading to variations in point density, spatial coverage, and alignment compared to the static state. Specifically, motion reduces the overlap between scans, causing certain regions to become sparse within the LiDAR's field of view, further complicating adaptation to dynamic conditions.

Mathematically, the input in the static training setup can be represented as

$$\mathbf{X}_{\text{train}} = \mathcal{P} \left( \sum_{i=1}^N \mathbf{R}_i(x, y, z) \right), \quad (3)$$

where  $\mathcal{P}()$  represents the projection operation mapping the 3D point cloud to a 2D reflectance image,  $\mathbf{R}_i(x, y, z)$  is the raw point cloud of the  $i$ -th scan,  $\sum$  denotes the geometric

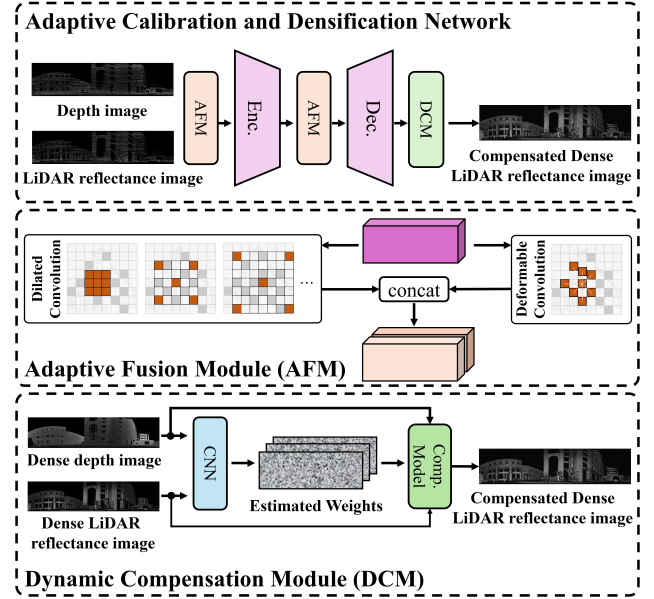


Fig. 6. Framework of the proposed method for LiDAR reflectance densification. The framework includes an Adaptive Feature Module (AFM) for feature extraction, an Encoder-Decoder structure for spatial reconstruction, and a Dynamic Compensation Module (DCM) to correct intensity.

merging of multi-scan point clouds. In contrast, the input to the training stage (also for the inference stage) when the robot is in motion is represented as

$$\mathbf{X}_{\text{test}} = \mathcal{P} \left( \sum_{i=1}^N \mathbf{T}_i \cdot \mathbf{R}_i(x, y, z) \right), \quad (4)$$

where  $\mathbf{T}_i$  is the transformation matrix derived from odometry, which introduces alignment errors. This misalignment results in a discrepancy between  $\mathbf{X}_{\text{train}}$  and  $\mathbf{X}_{\text{test}}$ , creating a domain gap. To address this, we propose a data augmentation method during training that simulates robot motions.

Specifically, during scan accumulation, random rotations and translations are applied to each scan to emulate motion-induced inconsistencies. For each scan in a sequence, the augmented input is represented as:

$$\mathbf{X}_{\text{aug}} = \mathcal{P} \left( \sum_{i=1}^N \mathbf{T}_{\text{motion}_j} (\mathbf{R}_i(x, y, z)) + \mathcal{N}(0, \sigma^2) \right), \quad (5)$$

where  $\mathcal{N}(0, \sigma^2)$  represents the Gaussian noise with a mean of 0 and variance  $\sigma^2$ , added to simulate sensor noise and motion variability. The transformation  $\mathbf{T}_{\text{motion}_j}$  applies a randomly predefined motion pattern  $j$ . To replicate the sparsity typically observed in real scenarios, we employ random scan sampling, where  $N$  scans are randomly selected from an initial sequence and then accumulated as input data. Furthermore, non-linear perturbations of odometry are introduced to emulate misaligned poses (e.g., acceleration discontinuities, sharp turns), while noisy IMU signals mimic errors from degraded sensors. By combining these augmentations, the proposed method improves the network's robustness to misaligned, sparse, and noisy inputs, effectively bridging the domain gap between static and dynamic motion conditions.



### C. Adaptive Calibration and Densification Network

Considering that convolutional neural networks (CNNs) effectively extract spatial features with computational complexity approximately proportional to the number of input elements  $\mathcal{O}(n)$  and maintain efficiency for large images, they were chosen as the backbone of our densification network. In contrast, Transformers [32], despite their strong modeling capabilities, exhibit a quadratic complexity of  $\mathcal{O}(n^2)$  with respect to the input size, which significantly limits their application in resource-constrained scenarios, especially for high-resolution images [33], [34]. Similarly, diffusion models [35], while demonstrating impressive performance in image restoration, rely on iterative processes to generate the final output, resulting in long inference times [36], making them hard for real-time robotics applications. Fig. 6 demonstrates the structure of our densification network, which employs a U-shaped architecture [37] where an Adaptive Fusion Module (AFM) and a Dynamic Compensation Module (DCM) are proposed to achieve densification. These modules address two key challenges: 1) adaptively fusing multi-scale information from non-uniform and sparse LiDAR scanning points and 2) mitigating the intensity decay that occurs with distance and incidence angle.

Let  $L_1 \in \mathbb{R}^{H \times W}$  and  $D_1 \in \mathbb{R}^{H \times W}$  are the LiDAR reflectance and depth images as the network input. The depth information is introduced in the reflectance image reconstruction during the reflectance compensation step. To maximize the utilization of cross-modal interaction and reduce model redundancy,  $L_1$  and  $D_1$  are first concatenated along the channel dimension as input to the network. Then, these inputs are processed through an encoder-decoder structure integrated with AFM to produce preliminary reconstructions of dense reflectance images  $L_2 \in \mathbb{R}^{H \times W}$  and depth images  $D_2 \in \mathbb{R}^{H \times W}$ , where the first and second channels of the decoder are  $L_2$  and  $D_2$ , respectively. Furthermore, to eliminate artifacts caused by signal intensity decay, the DCM is applied to compensate for these effects, resulting in the final dense LiDAR reflectance image  $L_3 \in \mathbb{R}^{H \times W}$ . The DCM employs a deep learning-based dynamic compensation model to avoid the complexity of manually designing the parameters required in traditional methods while maintaining end-to-end reconstruction.

**Encoder and Decoder.** The encoder has four stacked blocks, each comprising two sequentially connected layers with ReLU activation followed by an average pooling layer for downsampling. The convolutional kernels are set to a size of  $3 \times 3$ . The pooling window and stride of the pooling layer are configured with 2 for downsampling by a factor of 2. The decoder has a symmetric structure, comprising four decoder blocks. Within each decoder block, the input feature map is upsampled using a transposed convolution module. Subsequently, two  $3 \times 3$  convolutions are applied for local information fusion. To enhance multiscale feature integration, we implement two strategies: 1) an AFM module is inserted between the encoder and decoder to facilitate multi-scale spatial information; 2) similar to [37], features from

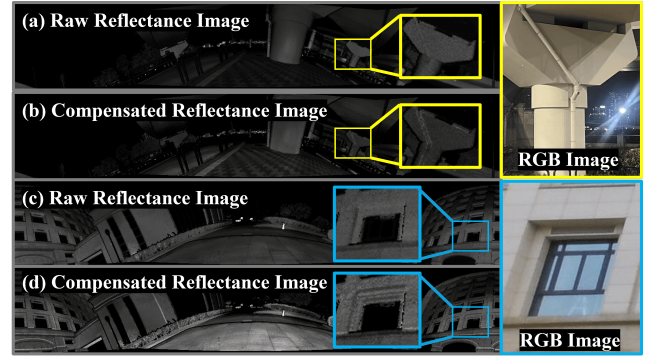


Fig. 7. Comparison between the raw dense reflectance and the compensated result. The compensated result maintains more consistent reflectance values for objects with the same surface material (yellow boxes in (a) and (b)) and exhibits clearer texture details (blue boxes in (c) and (d)).

the encoder are incorporated into the decoder. Corresponding feature maps of identical spatial dimensions from four blocks are concatenated to integrate multi-level information.

**Adaptive Fusion Module.** Due to the scanning characteristics of NRS-LiDAR, reflectance images captured in short durations are typically sparse and unevenly distributed. Besides, since objects in scenes possess multiscale attributes and vary in distance, fusing raw LiDAR reflectance data for incomplete information densification demands that the model possess adaptive capabilities and the ability to fuse multiscale structural features. Traditional convolutional kernels with limited receptive fields struggle to capture information across large regions, and larger kernels significantly increase computational cost. Inspired by [38], [39], we utilize parallel dilated convolutions and deformable convolutions to adaptively integrate multiscale information (Fig. 6). Specifically, we employ multiple dilation rates in parallel dilated convolutions to expand the receptive field with minimal additional computational cost, thereby enhancing the model's capacity for multiscale feature extraction. Simultaneously, we incorporate a deformable convolution to facilitate adaptive information fusion based on local contexts, thereby augmenting the model's ability to extract detailed information. The outputs from these parallel convolutions are subsequently concatenated along the channel dimension to form the output features of the AFM module.

**Dynamic Compensation Module.** The LiDAR intensity is primarily influenced by three factors: the distance traveled by light, the object's surface reflectance, and the incident angle of light. In general, it is assumed that the reflectance of the object's surface remains relatively consistent. Therefore, compensating for the effects of distance and incident angle is critical for intensity measurement [30]. As introduced in [30], the captured intensity can be expressed as

$$I(R, \alpha, \rho) \propto P(R, \alpha, \rho) = \eta(R) \frac{I_e \rho \cos \alpha}{R^2}, \quad (6)$$

where  $I_e$  represents the laser's emission power,  $R$  denotes the distance from the LiDAR to the object's surface,  $\alpha$  is the incident angle, and  $\rho$  indicates the surface reflectance of the object. The term  $\eta(R)$ , which accounts for the near-distance

TABLE I  
QUANTITATIVE COMPARISON OF DENSIFICATION PERFORMANCE

Method	PSNR / SSIM $\uparrow$	RMSE $\downarrow$	MAE $\downarrow$	Time (ms) $\downarrow$
IP-basic [40]	22.448 / 0.642	0.0672	0.0471	10.6 (CPU)
pNCNN [42]	25.746 / 0.718	0.0537	0.0282	168 (GPU)
Sparse-to-Dense [41]	26.277 / 0.724	0.0505	0.0272	69 (GPU)
Marigold-dc [43]	24.21 / 0.691	0.613	0.354	26140 (GPU)
Ours (w/o AFM)	26.051 / 0.721	0.0521	0.0276	<b>36</b> (GPU)
Ours (w/ AFM)	<b>27.152 / 0.767</b>	<b>0.0492</b>	<b>0.0247</b>	52 (GPU)

effect, can be expressed as

$$\eta(R) = 1 - \exp \left\{ -\frac{2r_d^2(R+d)^2}{D^2S_d^2} \right\}, \quad (7)$$

where  $r_d$  is the radius of the laser detector,  $d$  is the offset between the measured range and the true object distance,  $D$  is the lens diameter, and  $S_d$  is the focal length. At near distances,  $\eta(R)$  is small but increases rapidly as  $R$  grows, stabilizing near 1.0 for large  $R$ . Rearranging Eq. (6) to express  $I_e$  in terms of other variables:

$$I_c \approx I_e = C \frac{I(R, \alpha, \rho) \cdot R^2}{\eta(R) \cdot \rho \cos \alpha}, \quad (8)$$

where  $C$  is a proportionality constant that accounts for system-specific calibration factors.  $I_c$  represents the corrected or true intensity.

In practice, we collected data for objects with the same material under controlled angles and distances, fitted the required parameters by Eq. 8, and applied them to the raw dense LiDAR reflectance images to generate supervised compensated results. The compensated results are shown in Fig. 7. However, the above methods are further limited by data collection constraints and sensor configurations, making them inadequate for capturing complex, non-linear relationships in diverse environments. To address this, we use a simplified, parameterized compensation model, as shown in Eq. (9) and (10), which is based on Eq. (8) but incorporates an additional decay factor to comprehensively handle both near-distance and far-distance effects. For distance compensation, the distance correction factor  $\frac{R^2}{\eta(R)}$  becomes significantly large when  $R$  is large. Therefore, we approximated it using a second-order polynomial combined with an exponential decay factor to handle far-distance effects.

$$g(R) = \frac{(\alpha R^2 + \beta R + \gamma) \cdot \exp(-\lambda R)}{\eta(R)}, \quad (9)$$

where  $\alpha$ ,  $\beta$ ,  $\gamma$ , and  $\lambda$  are learnable parameters predicted dynamically by the network to capture the non-linear relationship between intensity and range.

For incidence-angle compensation, the intensity is normalized by  $\cos(\alpha)$ , following Lambert’s cosine law [44]. By combining both distance and angle compensation, the corrected intensity  $I_{\text{com}}$  is expressed as

$$I_{\text{com}} = \frac{I_m}{g(R) \cdot \cos(\alpha) \cdot \kappa}, \quad (10)$$

where  $I_m$  represents the measured intensity, equal to the  $I(R, \alpha, \rho)$  in Eq.6, and  $\kappa$  is a learnable parameter to account for variations in surface reflectance and sensor-specific factors. In our method, convolutional layers are used to dynamically predict the compensation parameters  $\alpha$ ,  $\beta$ ,  $\gamma$ ,  $\lambda$  and  $\kappa$  for each pixel based on local context, the distance

TABLE II  
QUANTITATIVE RESULTS OF DIFFERENT LOOP CLOSURE DETECTION METHODS IN DIFFERENT ENVIRONMENTS

Env.	Method	Detected Loops	True Positives	False Positives
Env. 1	ISC [46]	53	32 (60%)	21 (40%)
	IRIS [18]	36	19 (53%)	17 (47%)
	Ours	73	70 (96%)	3 (4%)
Env. 2	ISC [46]	88	59 (67%)	29 (33%)
	IRIS [18]	96	72 (75%)	24 (25%)
	Ours	138	130 (98%)	8 (2%)
Env. 3	ISC [46]	152	133 (88%)	19 (12%)
	IRIS [18]	162	78 (48%)	84 (52%)
	Ours	189	175 (93%)	14 (7%)

$R$  and the incident angle  $\alpha$  are both provided by  $D_2$ . These parameters are then applied to  $I_m$  using Eq. (10), enabling the model to perform intensity compensation.

## IV. EXPERIMENTS

We conducted a series of experiments to evaluate the effectiveness and robustness of the proposed method, focusing on the real-time LiDAR reflectance image densification and its applications in loop closure detection and traffic lane detection. Data collection and real-world experiments were conducted using a Livox MID-360, mounted on a Giraffe ground robot equipped with an NVIDIA RTX 3090 GPU and an Intel i7-1165G7 CPU. The experiments covered diverse scenarios, including varying lighting conditions (daylight, overcast, nighttime) and urban environments, to comprehensively evaluate the proposed method.

### A. Evaluation of LiDAR Reflectance Densification

To assess the performance of our proposed densification network, we conducted comparative and ablation experiments. Comparative experiments evaluated the quality of densified images generated by our method against CNN-based and traditional methods, both qualitatively and quantitatively. For qualitative evaluation, we visually compared the generated images with the results of competing methods (see Fig. 8). Quantitatively, we used standard metrics such as Peak Signal-to-Noise Ratio (PSNR), Structural Similarity Index Measure (SSIM), Root Mean Squared Error (RMSE), and Mean Absolute Error (MAE) to measure accuracy while also evaluating inference time to assess computational efficiency.

Since there are limited public datasets or few prior works specifically addressing reflectance densification, we trained several depth completion models and included traditional interpolation methods for comparison [40]–[43]. Additionally, an ablation study was conducted to analyze the contribution of the Adaptive Fusion Module (AFM). Table I presents the quantitative results, while Fig. 8 demonstrates the qualitative superiority of our method. Our method achieves high accuracy (highest PSNR/SSIM, lowest RMSE/MAE) while maintaining competitive runtime. Notably, as Marigold-dc [43] is a zero-shot diffusion-based method designed for depth completion, its performance is less effective in our task context; therefore, we only provide its quantitative results.

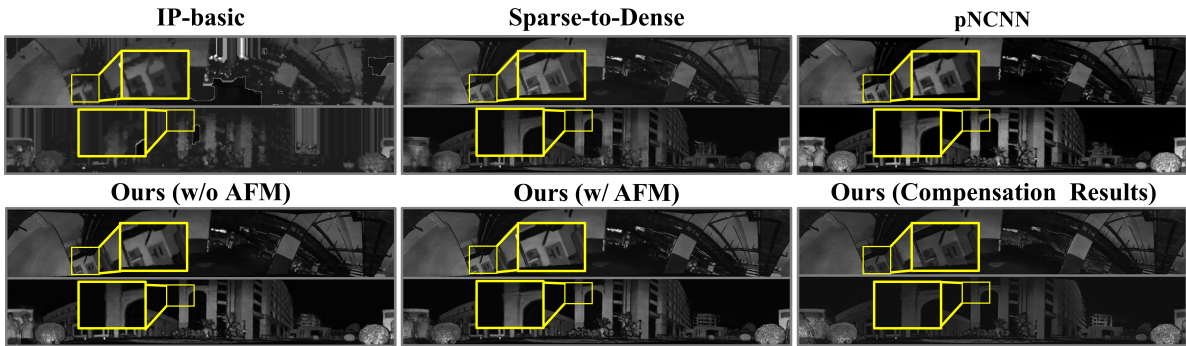


Fig. 8. Qualitative comparison of reflectance image densification across different methods in indoor and outdoor scenarios. IP-basic [40], which relies on non-learning techniques, struggles to recover structures in regions with large holes, resulting in distorted outputs. Furthermore, Sparse-to-Dense [41] and pNCNN [42] exhibit noticeable deficiencies in both smoothness and edge preservation. Our method with AFM demonstrates superior performance in preserving edge structures and enhancing details. The compensation results show that the intensity values for the same surface material (e.g., the same wall) are maintained more consistently (as shown in yellow boxes).

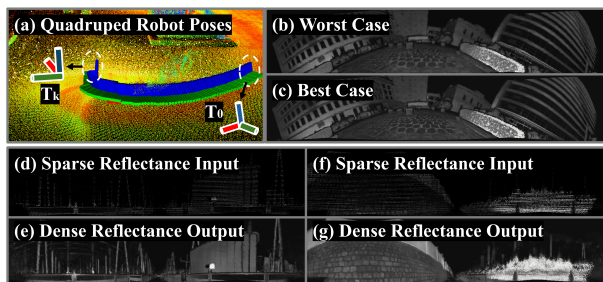


Fig. 9. (a)-(c) Densification results using 5-frame data with aggressive quadruped robot motion poses on uneven terrain, where (b) shows the worst case (PSNR = 25.75) and (c) shows the best case (PSNR = 26.82); (d)-(g) input and intensity image densification outputs on the public dataset [45].

To evaluate the performance of our method in generating dense reflectance images during robot motion, we tested on data (5-frame accumulation) captured when robot was subject to aggressive motion poses on uneven road. The resulting PSNR values (25.75–26.82) demonstrate the robustness of our approach against alignment noise and non-linear motion artifacts (Fig. 9). Additionally, we compared real-time results at various robot speeds in the supplementary material.

Although we wish to qualitatively evaluate the generalization ability of our method on the other datasets, to the best of our knowledge, we have not found such public datasets with dense ground truth. However, we show qualitative visualizations on a public dataset [45] (without dense ground truth), which can further validate the generalization ability of our approach, as illustrated in Fig. 9.

## B. Evaluation in Specific Applications

1) *Loop Closure Detection*: To validate the effectiveness of our method, we adopt the approach of [2] but replace the high-resolution reflectance data acquired by high-cost LiDAR with the dense reflectance images generated by our method using Livox MID-360. Specifically, [2] extracts ORB feature descriptors [47] from reflectance images for loop closure detection. These descriptors are then represented as bag-of-words vectors for querying loop closures. After retrieving a candidate match, ORB descriptor matching is performed, and outliers are removed using PnP RANSAC

[48] for verification. We conducted experiments in three distinct environments under two lighting conditions: daytime and nighttime (Fig. 10), using data collected under varying conditions to assess the generalization capability of our approach. Because the adopted loop closure detection method [2] is not based on deep learning, for a fair comparison, we compared our loop closure detection results with other non-deep-learning methods, including [18], [46], which are representative LiDAR-descriptor based methods. The results in Table II demonstrate that our method consistently outperforms competing approaches, maintaining reliable performance despite environmental and illumination changes.

2) *Traffic Lane Detection*: LiDAR reflectance images reveal a strong contrast between traffic lane markings and the road surface due to differences in physical material and surface properties. By leveraging the dense reflectance images generated by our method, we achieved accurate lane detection under diverse conditions, including very challenging scenarios for cameras (see Fig. 11). The lane detection was performed with LaneATT [49] as the baseline model. The model was trained on the TuSimple dataset [50] and fine-tuned on our dataset, which consists of 1,300 training images, 300 validation images, and 200 test images, with a maximum of four lanes per image. A ResNet-34 backbone [51] was used for fine-tuning the model. The detection performance was evaluated across three distinct environments with varying lighting conditions. The overall detection accuracy ranged from 93.3% to 96.1%, while the false detection rate (FDR) and false negative rate (FNR) remained low, with averages of 6.08% and 6.22%, respectively. The results show the robustness of our approach, which achieves stable and accurate lane detection, particularly under adverse lighting conditions (Fig. 11), outperforming camera-based methods.

## V. CONCLUSION

In this work, we introduce a novel benchmark dataset and a framework for generating dense LiDAR reflectance images from sparse measurements, addressing key challenges such as domain adaptation, intensity calibration, and reflectance restoration. Future work will explore generalizing our ap-



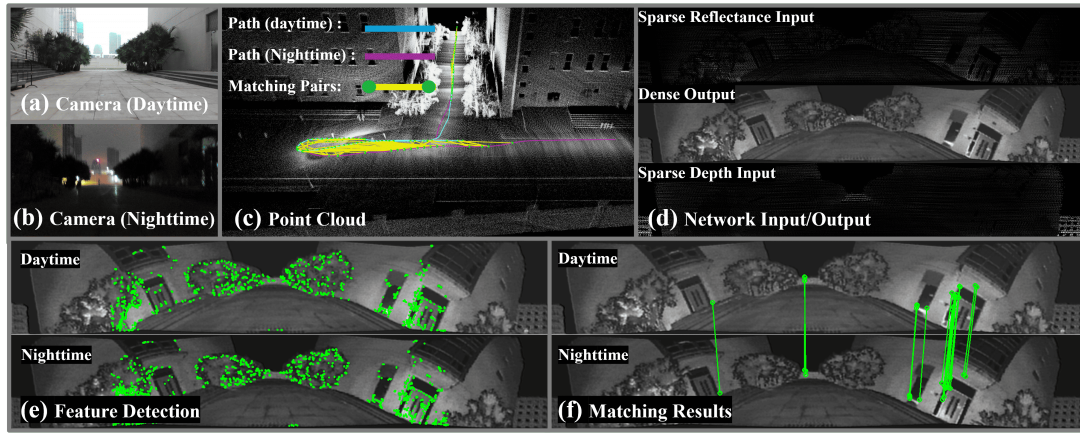


Fig. 10. Loop closure results across different times, with one dataset collected during daytime and the other at night (panoramic spherical projection). Our method achieves robust, real-time feature matching via visual loop closure detection, showing consistent performance under significant lighting variations.

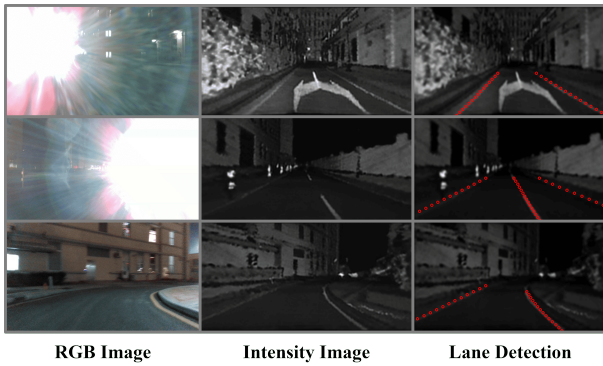


Fig. 11. Top: Single-lane scene with light pollution. Middle: Multi-lane scene with illumination from oncoming vehicles. Bottom: A curved road under insufficient lighting conditions.

proach to repeating-scanning LiDAR sensors and balancing real-time performance with densification quality. We also aim to leverage super-resolution reflectance images to enhance robotic perception in dynamic and challenging environments.

## REFERENCES

- [1] Patrick Pfrendschuh et al. Coin-lío: Complementary intensity-augmented lidar inertial odometry. In *ICRA*, pages 1730–1737, 2024.
- [2] Tixiao Shan et al. Robust place recognition using an imaging lidar. In *ICRA*, pages 5469–5475, 2021.
- [3] Jan Wietrzykowski and Piotr Skrzypczyński. Descriptive power of lidar intensity images for loop closing. In *IROS*, pages 79–85, 2021.
- [4] Luca Di Giammarino et al. Visual place recognition using lidar intensity. In *IROS*, pages 4382–4389, 2021.
- [5] Yanfeng Zhang et al. Ri-lío: Reflectivity image assisted tightly-coupled lidar-inertial odometry. *IEEE RA-L*, 8(3):1802–1809, 2023.
- [6] Wenqiang Du and Giovanni Beltrame. Real-time slam with lidar intensity. In *ICRA*, pages 4164–4170, 2023.
- [7] Mohammad Aldibaja et al. Intensity-based localization on snow-wet roads. *IEEE TII*, 13(5):2369–2378, 2017.
- [8] Christophe Reymann and Simon Lacroix. Improving lidar classification using intensities. In *IROS*, pages 5122–5128, 2015.
- [9] Kasi Viswanath et al. Reflectivity is all you need!: Advancing lidar segmentation. *arXiv preprint*, 2024.
- [10] Alberto Hata and Denis Wolf. Road marking detection using lidar intensity. In *ITSC*, pages 584–589, 2014.
- [11] Xiaolu Li et al. Lidar intensity correction for road marking detection. *Optics and Lasers in Engineering*, 160:107240, 2023.
- [12] Weichen Dai et al. Lidar intensity completion: Fully exploiting sensor messages. *Sensors*, 22(19):7533, 2022.
- [13] Li Li et al. Durlar: High-fidelity lidar dataset for autonomous driving. In *3DV*, pages 1227–1237, 2021.
- [14] Charles R Qi et al. Pointnet: Deep learning on point sets for 3d classification and segmentation. In *CVPR*, pages 652–660, 2017.
- [15] Wei Xu et al. Fast-lío2: Fast direct lidar-inertial odometry. *IEEE T-RO*, 38(4):2053–2073, 2022.
- [16] David Wisht et al. Vilens: Visual, inertial, lidar, and leg odometry for all-terrain legged robots. *IEEE T-RO*, 39(1):309–326, 2022.
- [17] Jiarong Lin et al. R3live: A robust, real-time, rgb-colored, lidar-inertial-visual tightly-coupled state estimation. In *ICRA*, pages 10672–10678, 2022.
- [18] Ying Wang et al. Lidar iris for loop-closure detection. In *IROS*, pages 5769–5775, 2020.
- [19] Wei Gao et al. Active loop closure for osm-guided robotic mapping in large-scale urban environments. In *IROS*, pages 12302–12309, 2024.
- [20] Jonas Uhrig et al. Sparsity invariant cnns. In *3DV*, pages 11–20, 2017.
- [21] Fangchang Ma and Sertac Karaman. Sparse-to-dense: Depth prediction from sparse samples. In *ICRA*, pages 4796–4803, 2018.
- [22] Jiaxiong Qiu et al. Deeplidar: Depth prediction for sparse lidar. In *CVPR*, pages 3313–3322, 2019.
- [23] Kaiyue Lu et al. Depth completion via auxiliary image reconstruction. In *CVPR*, pages 11306–11315, 2020.
- [24] Qingyang Yu et al. Grayscale and normal guided depth completion. In *ICIP*, pages 979–983, 2021.
- [25] Tian Yu Liu et al. Monitored distillation for depth completion. In *ECCV*, pages 35–53, 2022.
- [26] Xingxing Zuo et al. Codevio: Visual-inertial odometry with dense depth. In *ICRA*, pages 14382–14388, 2021.
- [27] Mingle Zhao et al. Dit-slam: Dense visual-inertial slam with implicit depth. *Sensors*, 22(9):3389, 2022.
- [28] Guangkai Xu et al. Towards domain-agnostic depth completion. *Machine Intelligence Research*, 21(4):652–669, 2024.
- [29] Jin-Hwi Park et al. Depth prompting for sensor-agnostic depth estimation. In *CVPR*, pages 9859–9869, 2024.
- [30] Wei Fang et al. Intensity correction of terrestrial laser scanning data. *IEEE TGRS*, 53(2):942–951, 2014.
- [31] Huajie Wu et al. Moving event detection from lidar point streams. *Nature Communications*, 15(1):345, 2024.
- [32] Ashish Vaswani et al. Attention is all you need. *NeurIPS*, 30, 2017.
- [33] Syed Waqas Zamir et al. Restormer: Transformer for high-resolution image restoration. In *CVPR*, pages 5728–5739, 2022.
- [34] Jingyun Liang et al. Swinir: Image restoration using swin transformer. In *ICCV*, pages 1833–1844, 2021.
- [35] Jonathan Ho et al. Denoising diffusion probabilistic models. *NeurIPS*, 33:6840–6851, 2020.
- [36] Xin Li et al. Diffusion models for image restoration and enhancement: A survey. *arXiv preprint*, 2023.
- [37] Olaf Ronneberger et al. U-net: Convolutional networks for biomedical image segmentation. In *MICCAI*, pages 234–241, 2015.
- [38] Liang-Chieh Chen et al. Deeplab: Semantic image segmentation with deep nets and crfs. *IEEE TPAMI*, 40(4):834–848, 2017.
- [39] Shu Kong et al. Recurrent scene parsing with perspective understanding in the loop. In *CVPR*, pages 956–965, 2018.
- [40] Jason Ku et al. In defense of classical image processing for depth completion. In *CRV*, pages 16–22, 2018.



- [41] Fangchang Ma et al. Self-supervised sparse-to-dense depth completion. In *ICRA*, pages 3288–3295, 2019.
- [42] Abdelrahman Eldesokey et al. Uncertainty-aware cnns for depth completion. In *CVPR*, pages 12014–12023, 2020.
- [43] Massimiliano Viola et al. Marigold-dc: Zero-shot monocular depth completion with guided diffusion. *arXiv preprint arXiv:2412.13389*, 2024.
- [44] Sanna Kaasalainen et al. Incidence angle effects on laser scanner intensity. *Remote Sensing*, 3(10):2207–2221, 2011.
- [45] Yanbo Wang et al. Sfpnet: Sparse focal point network for lidar segmentation. In *ECCV*, 2024.
- [46] Han Wang et al. Intensity scan context: Coding intensity and geometry relations for loop closure detection. In *ICRA*, pages 2095–2101, 2020.
- [47] Ethan Rublee et al. Orb: Alternative to sift or surf. In *ICCV*, pages 2564–2571, 2011.
- [48] Martin A Fischler and Robert C Bolles. Random sample consensus: a paradigm for model fitting with applications to image analysis and automated cartography. *Communications of the ACM*, 1981.
- [49] Lucas Tabelini et al. Keep your eyes on the lane: Real-time attention-guided lane detection. In *CVPR*, pages 294–302, 2021.
- [50] Tusimple lane detection challenge. <https://github.com/TuSimple/tusimple-benchmark>, 2017.
- [51] Kaiming He et al. Deep residual learning for image recognition. In *CVPR*, pages 770–778, 2016.

# Super LiDAR Reflectance for Robotic Perception

## Supplementary Material

### VI. LiDAR REFLECTANCE COMPENSATION

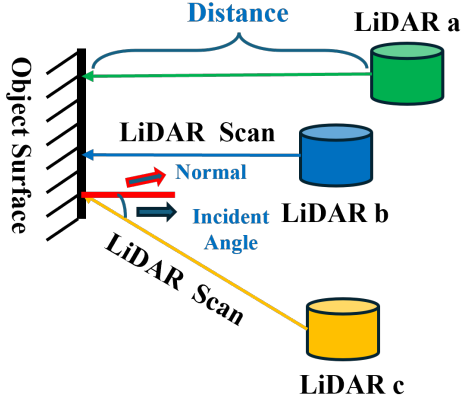


Fig. 12. For the same object, LiDAR reflectance differs between a and b due to distance, and between a and c due to angle.

As shown in Fig. 12, for the same object, the reflectance obtained by the LiDAR beam varies due to differences in distance or incidence angle. In practice, multiple datasets are collected for objects of the same material, where distance and angle are controlled as single variables to fit their respective relationships with reflectance. The model parameters are then obtained based on the formula in the text. An example of the calibration results is shown in Fig. 13, after applying our compensation method, the reflectance for the same object remain consistent (see Fig. 13 (b)), unlike in Fig. 13 (a), where the reflectance varies with incidence angle or distance. Furthermore, to validate the effectiveness of our compensation model at long distances (greater than 10m), we analyzed the intensity distribution of the same object across different distances and angles, along with the corrected results, as shown in Fig. 14. The results demonstrate that our compensation method effectively maintains the reflectance values within a consistent range across varying distances and angles for the same object.

### VII. SUPPLEMENTARY EXPERIMENTS

#### A. Test on Pubic Dataset

As mentioned in Section IV-A, we provide more qualitative visualizations results on a public dataset [45] (without dense ground truth), which can further validate the generalization ability of our approach, as illustrated in Fig. 15.

#### B. Impact of Frame Accumulation on Densification Quality

As mentioned in Section IX, to justify the rationale behind using 5-frame accumulated data as input for our method, we qualitatively and quantitatively compared the densification

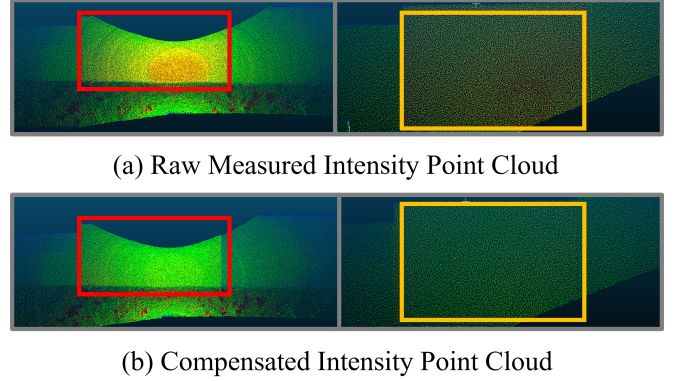


Fig. 13. For the same object (red and orange boxes), raw measurements show inconsistencies in reflectance due to variations in angle and distance (color represents reflectance values). After compensation, the reflectance for the same object in the point cloud is maintained within a consistent range.

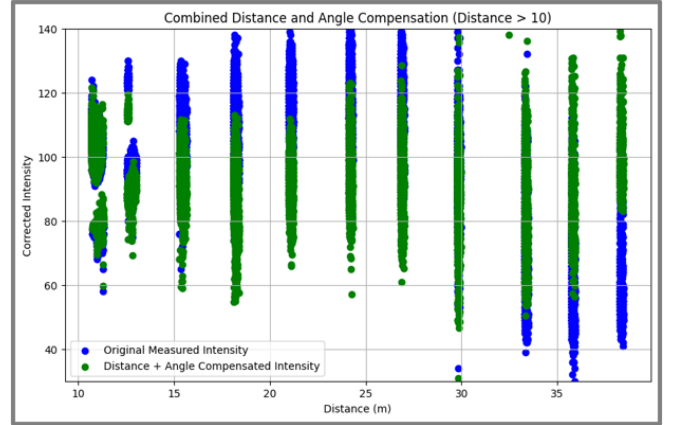


Fig. 14. Reflectance values distributed across different distances. Blue points represent the original measured intensity, showing significant variation with distance, while green points represent the values after applying our compensation model, maintaining a more consistent range.

results by using the single-frame and 10-frame accumulated data as input. As shown in Table III and Fig. 16, the densification performance of 5-frame input is comparable to that of 10-frame input, while the reconstruction quality of single-frame input is significantly worse. This is because single-frame input is often excessively sparse, resulting in objects lacking sufficient information for accurate reconstruction. It is worth noting that the evaluation here is based on the densification quality of statically collected data. Although the 10-frame input achieves better metric performance, it overlooks the impact of odometry errors and moving objects in the scene during the robot's motion. The input data and the generated images are illustrated in Fig. 16.



Fig. 15. Input and intensity image densification results on the public dataset [45]

TABLE III  
QUANTITATIVE COMPARISON OF DENSE REFLECTANCE IMAGES  
GENERATED FROM 1-FRAME, 5-FRAME, AND 10-FRAME ACCUMULATED  
INPUT USING DIFFERENT METRICS

Frames Input	PSNR	SSIM	RMSE	MAE
1-frame	22.303	0.350	0.0802	0.058
5-frame	27.142	0.757	0.0503	0.0263
10-frame	27.239	0.762	0.0496	0.0256

### C. Impact of Robot Speed on Densification Performance

Considering that our method is designed to serve the perception tasks of robots during motion, we conducted experiments to evaluate the dynamic densification results at different robot speeds in the same scenarios, using loop closure detection as the test task. The quantitative comparison results are shown in Table IV. Two visual loop closure detection results, as well as the generated image quality and feature point matching results at different speeds, are illustrated in Fig. 17.

TABLE IV  
LOOP CLOSURE DETECTION RESULTS UNDER DIFFERENT SPEEDS

Average Speed (m/s)	Detected Loops	Trajectory Length (m)
0.73	213	193.73
1.52	185	203.51

## VIII. DATASET CONSTRUCTION

We constructed the Super LiDAR Reflectance dataset, which includes 1,000 raw ROS packets and an additional 5,000 sets of reflectance images with configurations ranging from sparse (1 scan) to dense (500 scans). Specifically, from the 1,000 raw ROS packets, 1,000 panoramic reflectance images were generated using the panoramic mode projection, with some exemplar results shown in Fig. 18. These images cover the full field of view (FoV) of the LiDAR sensor. Similarly, 4,000 sets of reflectance images were generated from the same 1,000 raw ROS packets using the virtual-camera projection mode, with exemplar images shown in Fig. 19.

Furthermore, the dataset contains two subsets tailored for practical tasks. The first subset is designed to evaluate the performance of generated panoramic dense reflectance images in loop closure detection. The second subset assesses the utility of generated virtual-camera dense reflectance images for traffic lane detection. Both subsets were collected while the robot was in motion, aiming to validate the effectiveness of dense reflectance images in enhancing perception during robot movement.

## IX. LIMITATION AND FUTURE WORK

While the proposed method demonstrates significant advancements in generating dense LiDAR reflectance images, several limitations remain. First, the current approach is not easily generalizable to all LiDAR types due to differences in scanning patterns, which limits its adaptability across various hardware setups. Future work will investigate the generalization and adaptability of the method to LiDAR with different scanning modes to address this limitation.

Second, the use of single-frame input helps mitigate the static-to-dynamic domain gap issue but results in excessively sparse data, which can impact performance. Addressing this trade-off is an important direction for future work to further enhance the method's robustness and performance, particularly in dynamic and challenging environments.

In addition, this paper presents a novel method for generating dense LiDAR reflectance images from sparse input, addressing challenges such as domain adaptation, intensity calibration, and restoration. In the future, we will leverage the generated super LiDAR reflectance images to support a wider range of robotic perception tasks, enabling their use in dynamic and complex environments.

Moreover, the integration of camera images with LiDAR reflectance images will be explored. By coloring reflectance images with camera information, the densified images can provide more detailed semantic understanding, bridging the gap between LiDAR and camera domains. This will open up new possibilities for vision-based tasks, such as semantic segmentation, where camera-based methods can be adapted to operate on LiDAR data. These advancements will further expand the applicability of the proposed method in diverse robotic perception scenarios.

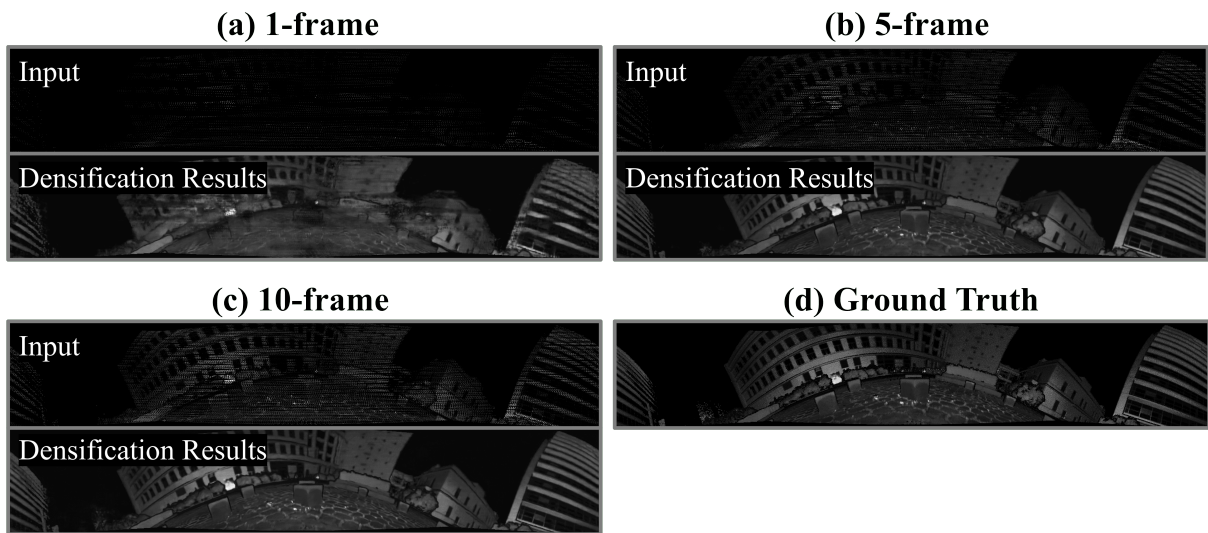


Fig. 16. Comparison of dense reflectance image generated from 1-frame, 5-frame, and 10-frame accumulated input

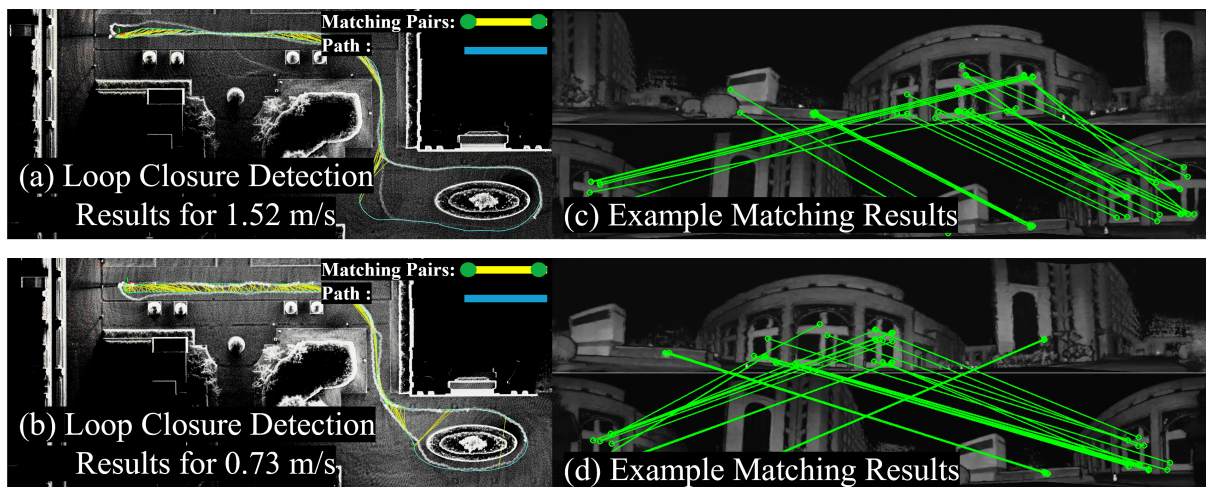


Fig. 17. Loop closure detection and feature point matching results at different robot speeds in the same scene.



Fig. 18. Panoramic reflectance images generated using panoramic projection.





Fig. 19. Virtual-camera reflectance images generated using virtual-camera projection.